Frontier Molecular Orbital Contributions to Chlorination versus Hydroxylation Selectivity in the Non-Heme Iron Halogenase SyrB2

Martin Srnec[#], Edward I. Solomon[†]

Department of Chemistry, Stanford University, Stanford, CA 94305-5080, U. S. A., J. Heyrovský Institute of Physical Chemistry, The Czech Academy of Sciences, Czech Republic

Supporting Information

[#] J. Heyrovský Institute of Physical Chemistry, The Czech Academy of Sciences, Czech Republic

[†] Stanford University, USA

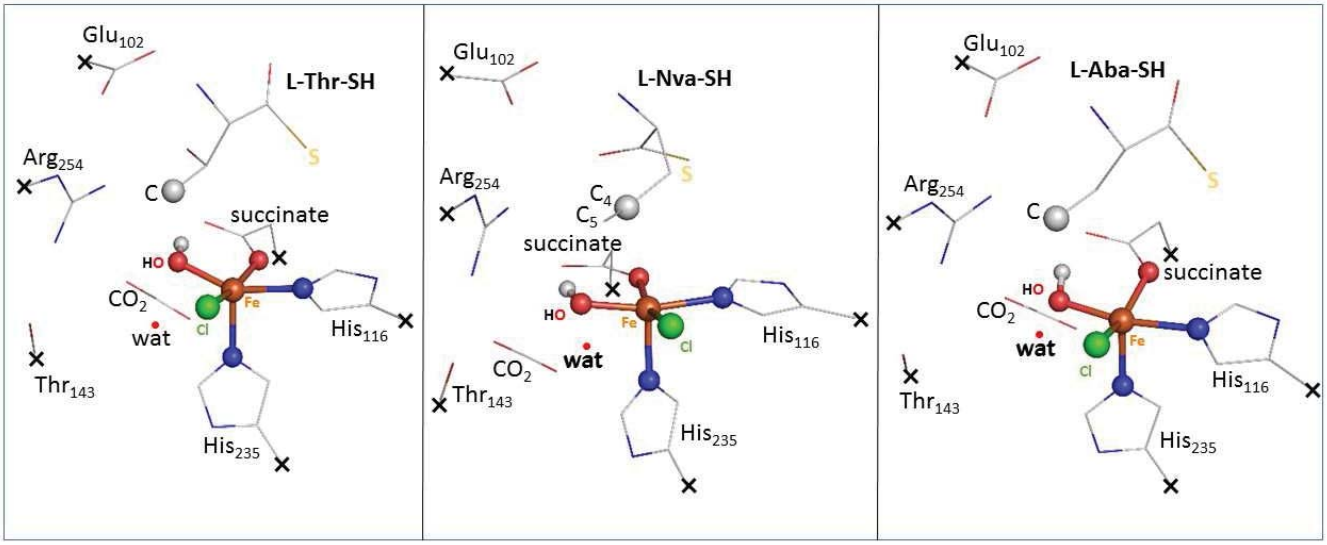

Figure S1A. Structural models of the active site of SyrB2 in the presence of three different substrates. The crosses indicate the atoms fixed at the crystallographic positions (taken from ref 4 in the main text). For clarity, the hydrogen atoms are not displayed. The S atom of a substrate was fixed at the position determined in ref 6 (the main text) using a molecular docking procedure (ref 15 in the main text).

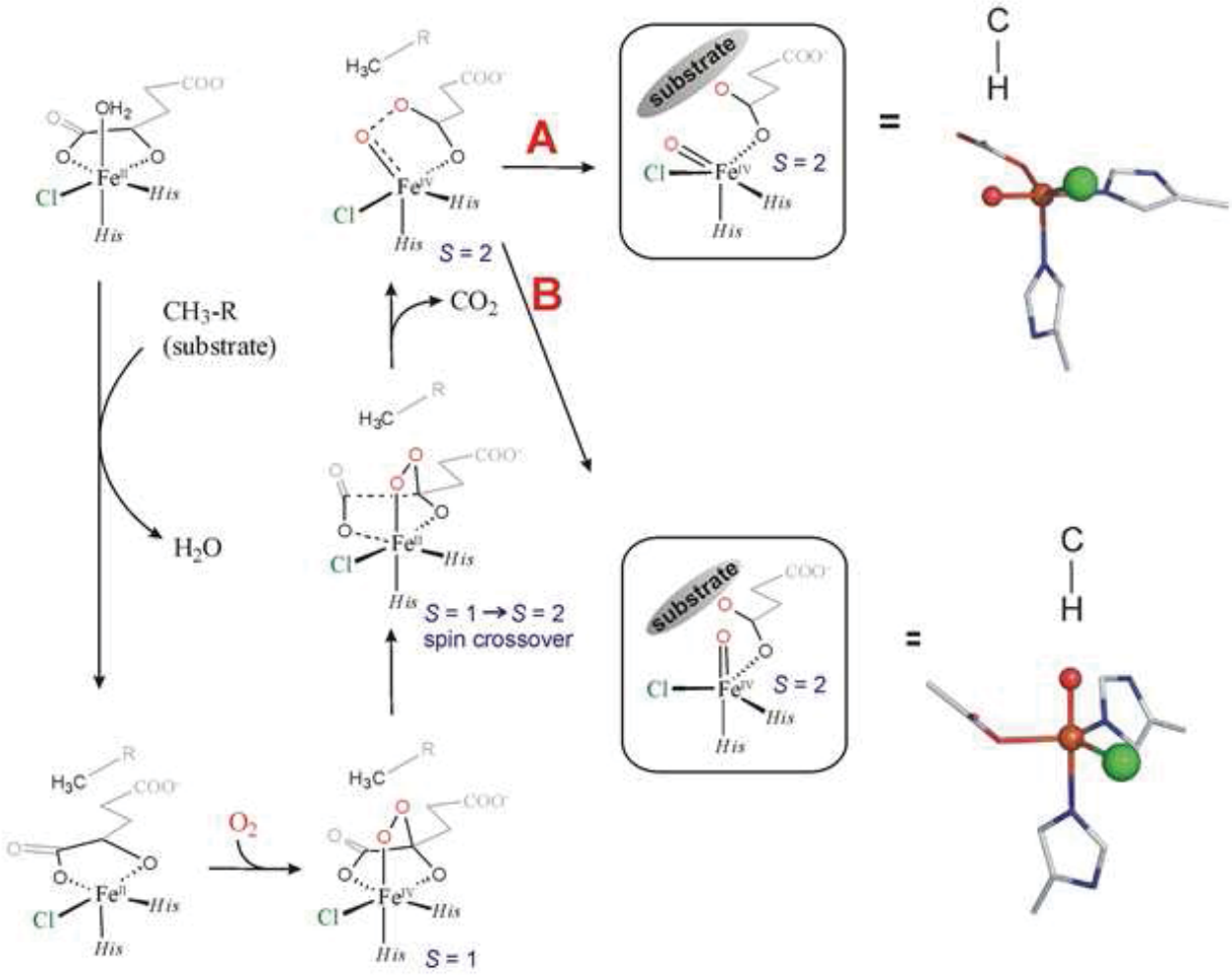

The Fe^{IV}=O bond resulting from O_2 activation can be oriented into or away from the substrate cavity, depending on whether the O_2 moiety upon O_2 activation interacts with a substrate through a hydrogen bond:

A - no H-bond interaction between the substrate & O_2

→ **rotation** of the Fe–O–O–O ring that leads to the π-orientation of the C—H bond w/ respect to the Fe^{IV}=O.

B - an H-bond interaction between the substrate & O_2

→ **no rotation** of the Fe–O–O–O ring that leads to the σ-orientation of the C—H bond w/ respect to the Fe^{IV}=O.

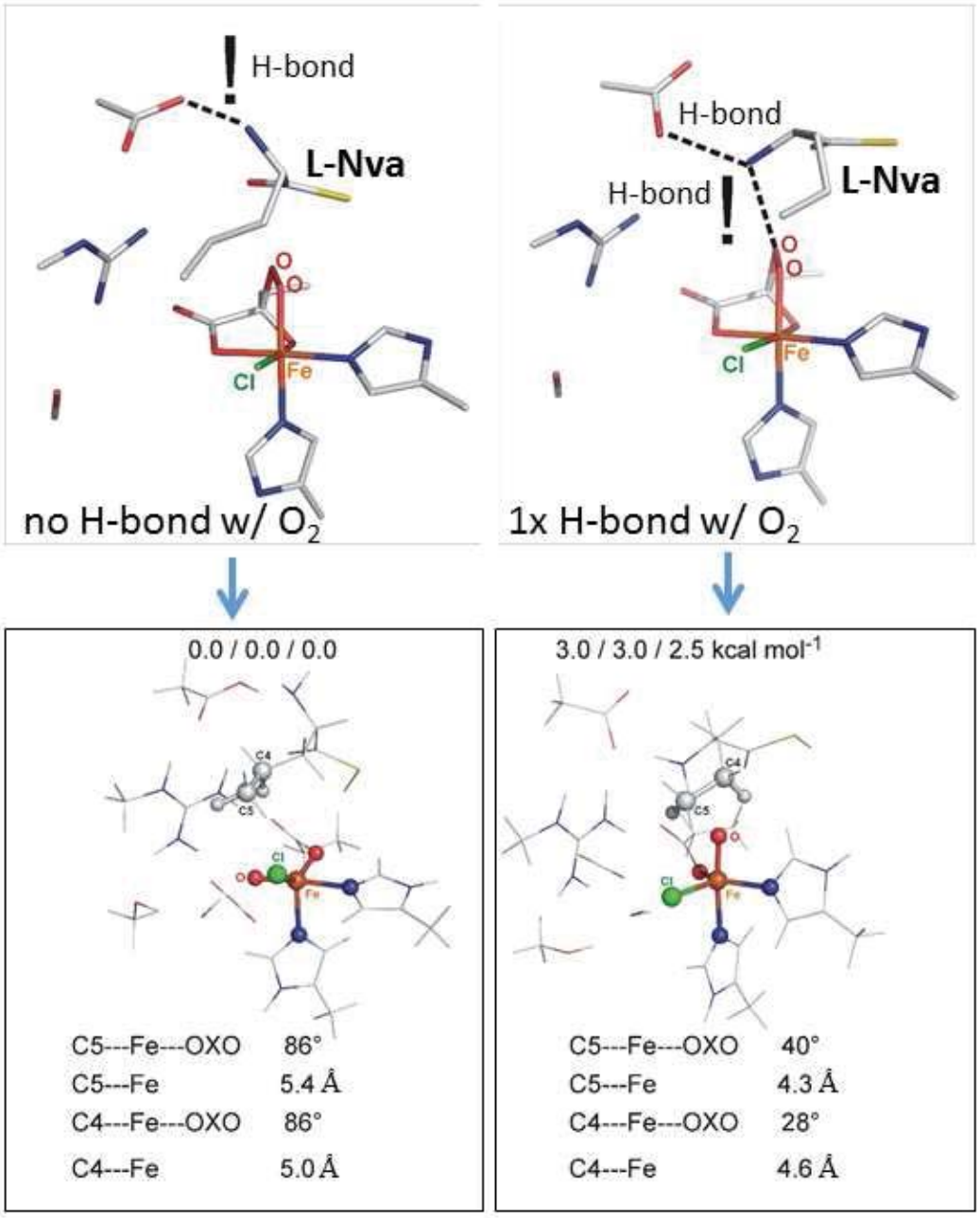

Figure S1B. Preceding page: the O_2 activation pathway as suggested in ref 6. This page: The peroxy-bridged $S = 1$ Fe^{IV} intermediate in the presence of the substrate L-Nva that fits the protein cavity with two different conformations (one with no H-bond to O_2 moiety (*left*) and one with an H-bond to O_2 (*right*)). Starting from these two different peroxy-bridged complexes, the Fe^{IV}=O products of O_2 activation have two different orientations with the oxo oriented toward and away from the substrate. The structure with oxo oriented away from the substrate cavity is ~3 kcal mol^{-1} lower in energy.

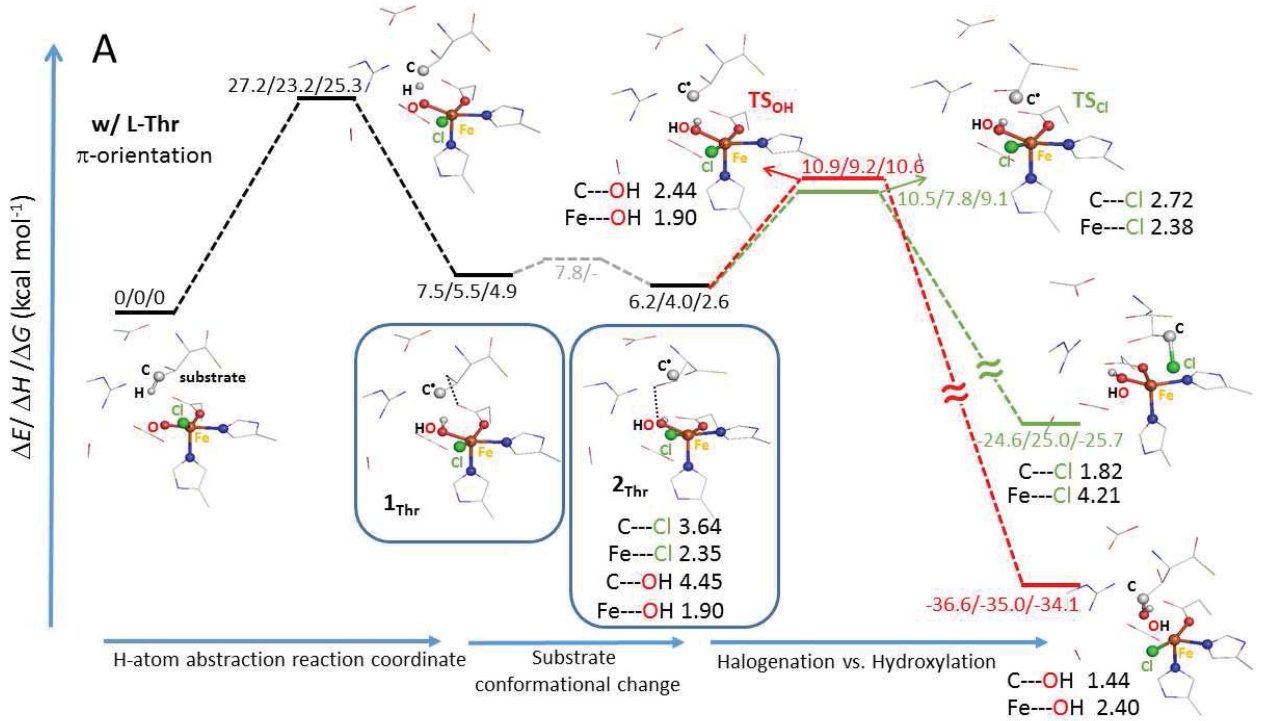
A
w/ L-Thr
π-orientation
ΔE/ ΔH /ΔG (kcal mol-1)
27.2/23.2/25.3
0/0/0
7.5/5.5/4.9
7.8/-
6.2/4.0/2.6
substrate
1Thr
2Thr
C---OH 3.64
Fe---Cl 2.35
C---OH 4.45
Fe---OH 1.90
TSOH
C---OH 2.44
Fe---OH 1.90
10.9/9.2/10.6
10.5/7.8/9.1
TSCl
C---Cl 2.72
Fe---Cl 2.38
-24.6/25.0/-25.7
C---Cl 1.82
Fe---Cl 4.21
-36.6/-35.0/-34.1
C---OH 1.44
Fe---OH 2.40
H-atom abstraction reaction coordinate
Substrate
conformational change
Halogenation vs. Hydroxylation

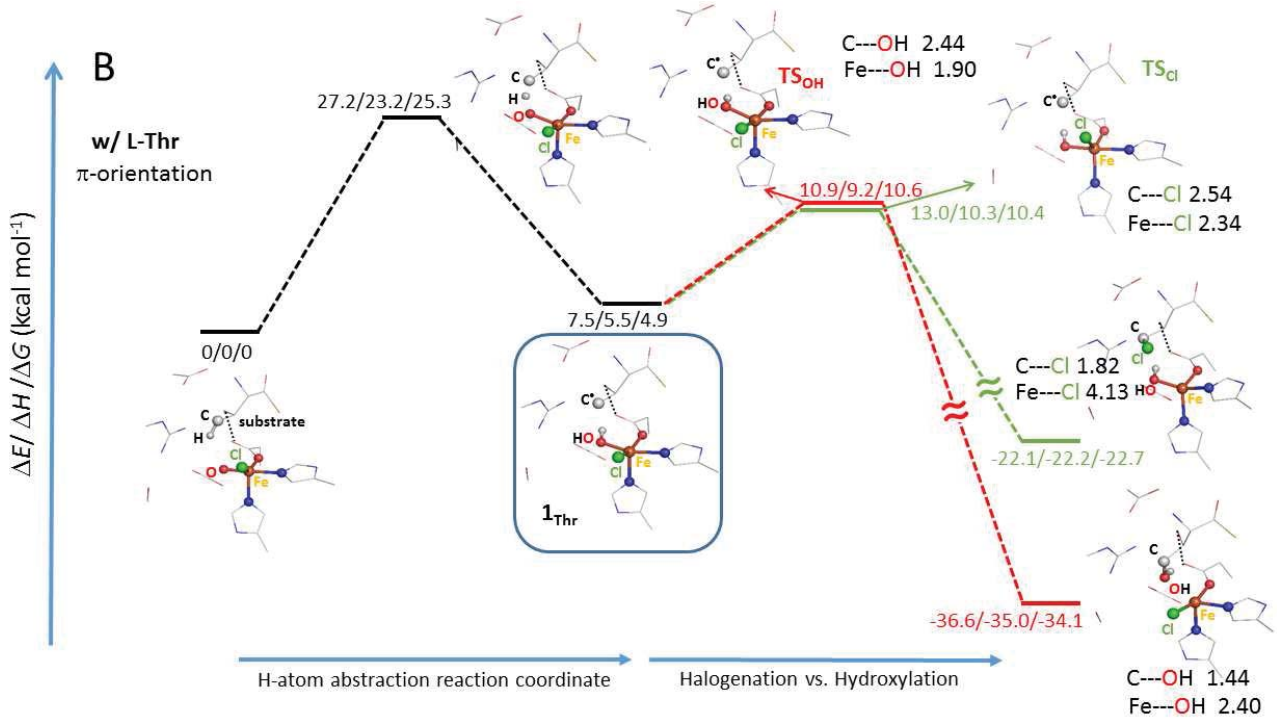
B
w/ L-Thr
π-orientation
ΔE/ ΔH /ΔG (kcal mol-1)
27.2/23.2/25.3
0/0/0
7.5/5.5/4.9
substrate
1Thr
TSOH
C---OH 2.44
Fe---OH 1.90
10.9/9.2/10.6
13.0/10.3/10.4
TSCl
C---Cl 2.54
Fe---Cl 2.34
C---Cl 1.82
Fe---Cl 4.13
-22.1/-22.2/-22.7
-36.6/-35.0/-34.1
C---OH 1.44
Fe---OH 2.40
H-atom abstraction reaction coordinate
Halogenation vs. Hydroxylation

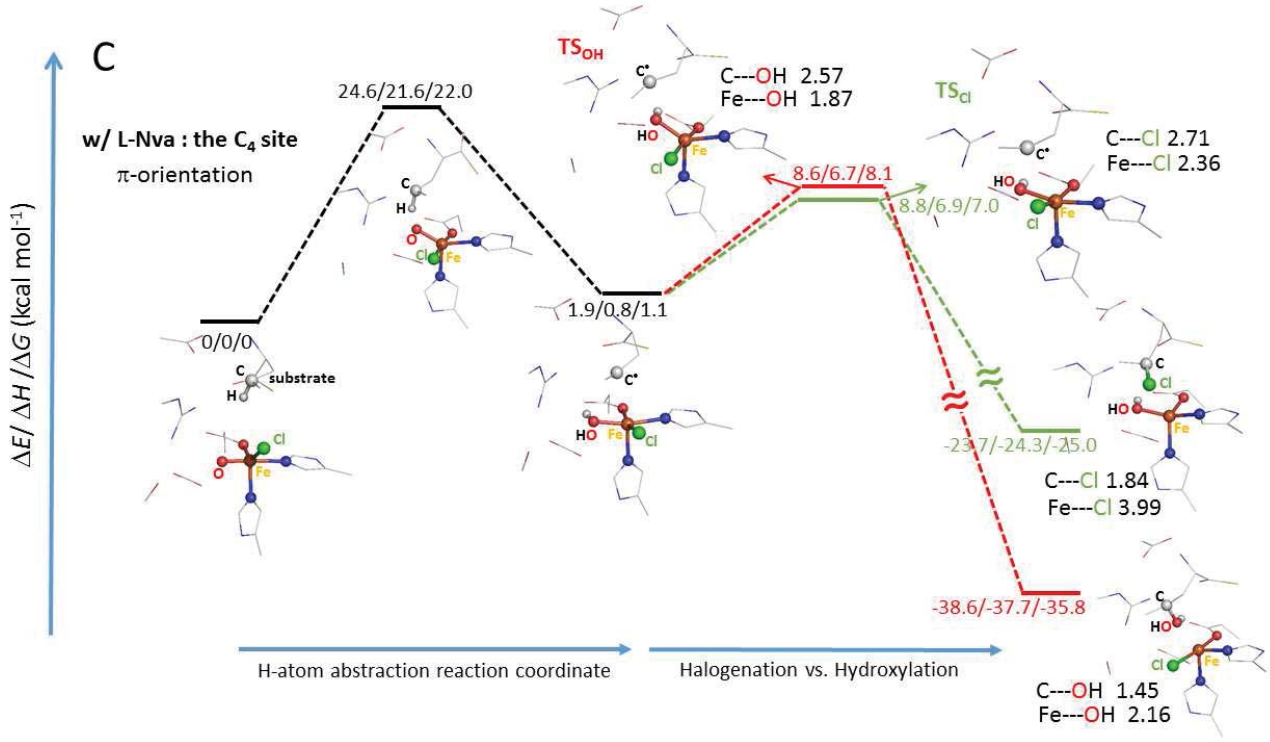
C
w/ L-Nva : the C4 site
π-orientation
ΔE/ ΔH /ΔG (kcal mol-1)
24.6/21.6/22.0
0/0/0
substrate
TSOH
C---OH 2.57
Fe---OH 1.87
1.9/0.8/1.1
8.6/6.7/8.1
TSCl
C---Cl 2.71
Fe---Cl 2.36
8.8/6.9/7.0
-23.7/-24.3/-25.0
C---Cl 1.84
Fe---Cl 3.99
-38.6/-37.7/-35.8
C---OH 1.45
Fe---OH 2.16
H-atom abstraction reaction coordinate
Halogenation vs. Hydroxylation

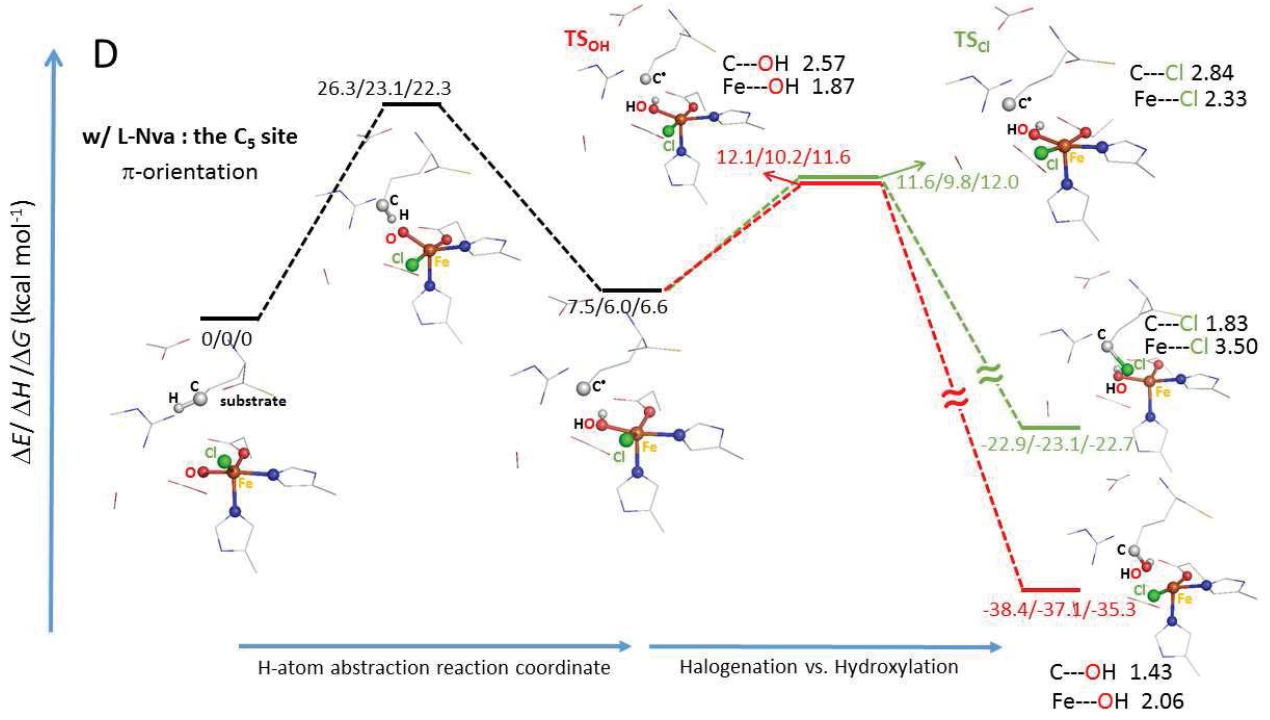
D
w/ L-Nva : the C5 site
π-orientation
ΔE/ ΔH /ΔG (kcal mol-1)
26.3/23.1/22.3
0/0/0
substrate
TSOH
C---OH 2.57
Fe---OH 1.87
7.5/6.0/6.6
12.1/10.2/11.6
TSCl
C---Cl 2.84
Fe---Cl 2.33
11.6/9.8/12.0
C---Cl 1.83
Fe---Cl 3.50
-22.9/-23.1/-22.7
-38.4/-37.1/-35.3
C---OH 1.43
Fe---OH 2.06
H-atom abstraction reaction coordinate
Halogenation vs. Hydroxylation

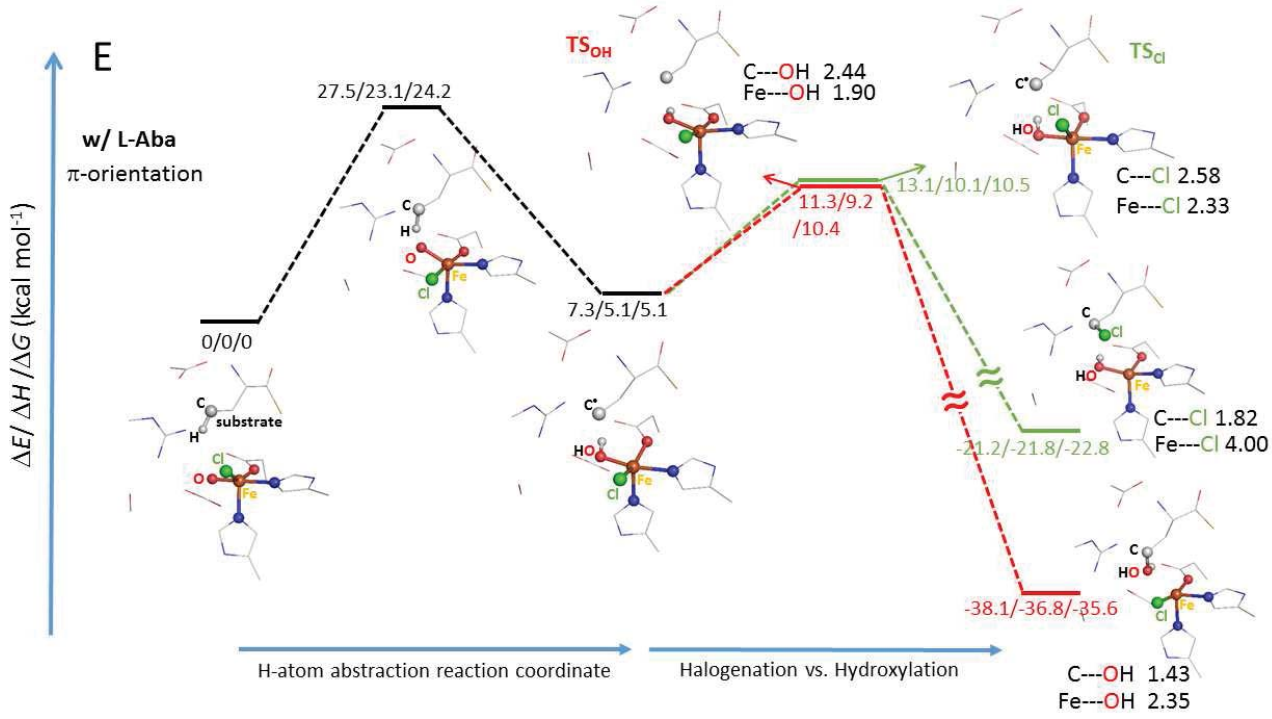
E
w/ L-Aba
π-orientation
ΔE/ ΔH /ΔG (kcal mol-1)
27.5/23.1/24.2
0/0/0
substrate
7.3/5.1/5.1
TSOH
C---OH 2.44
Fe---OH 1.90
11.3/9.2
/10.4
13.1/10.1/10.5
TSCl
C---Cl 2.58
Fe---Cl 2.33
-21.2/-21.8/-22.8
C---Cl 1.82
Fe---Cl 4.00
-38.1/-36.8/-35.6
C---OH 1.43
Fe---OH 2.35
H-atom abstraction reaction coordinate
Halogenation vs. Hydroxylation

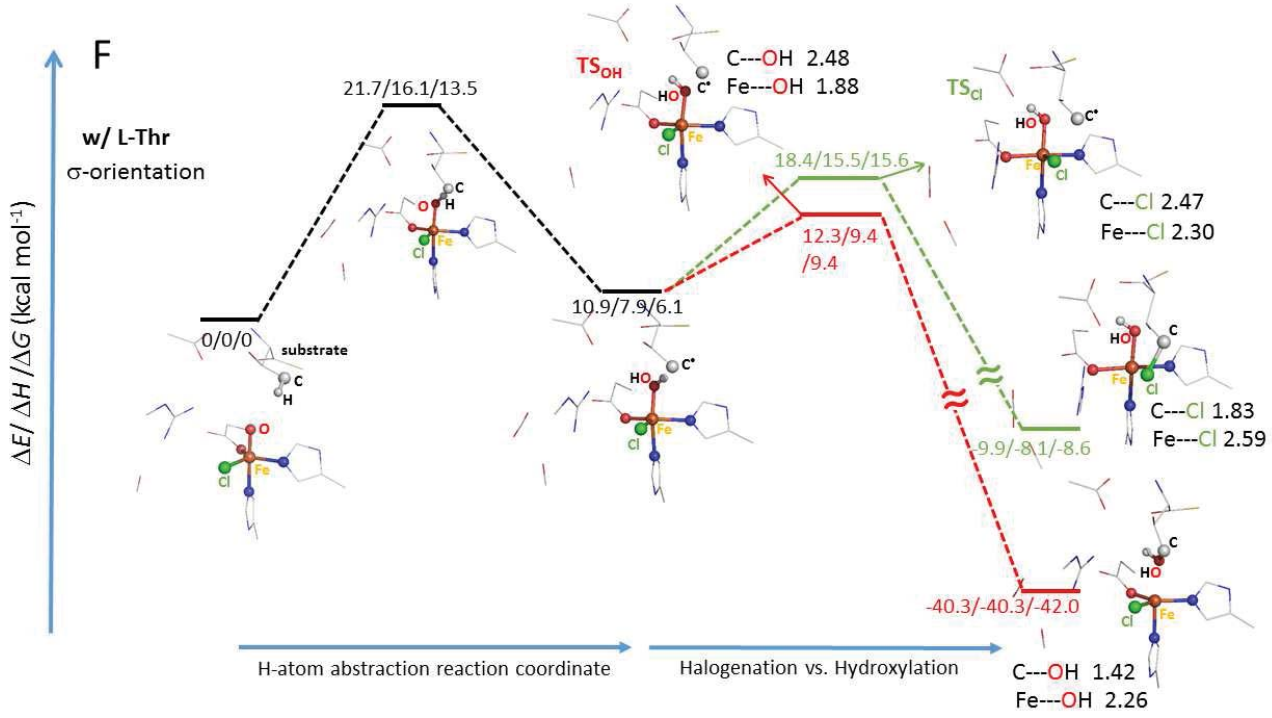
F
w/ L-Thr
σ-orientation
ΔE/ ΔH /ΔG (kcal mol-1)
21.7/16.1/13.5
0/0/0
substrate
10.9/7.9/6.1
TSOH
C---OH 2.48
Fe---OH 1.88
12.3/9.4
/9.4
18.4/15.5/15.6
TSCl
C---Cl 2.47
Fe---Cl 2.30
-9.9/-8.1/-8.6
C---Cl 1.83
Fe---Cl 2.59
-40.3/-40.3/-42.0
C---OH 1.42
Fe---OH 2.26
H-atom abstraction reaction coordinate
Halogenation vs. Hydroxylation

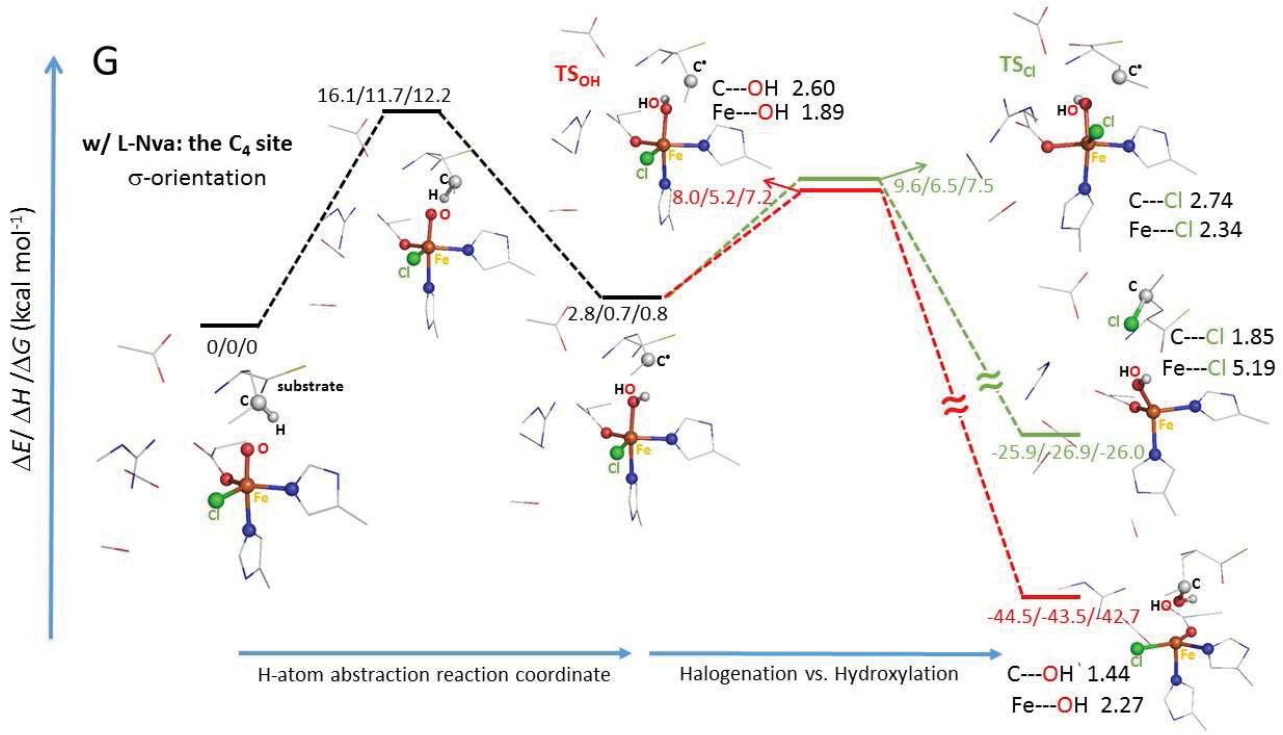
G
w/ L-Nva: the C4 site
σ-orientation
ΔE/ ΔH /ΔG (kcal mol-1)
16.1/11.7/12.2
0/0/0
substrate
TSOH
C---OH 2.60
Fe---OH 1.89
8.0/5.2/7.2
2.8/0.7/0.8
9.6/6.5/7.5
TSCl
C---Cl 2.74
Fe---Cl 2.34
C---Cl 1.85
Fe---Cl 5.19
-25.9/-26.9/-26.0
-44.5/-43.5/-42.7
C---OH 1.44
Fe---OH 2.27
H-atom abstraction reaction coordinate
Halogenation vs. Hydroxylation

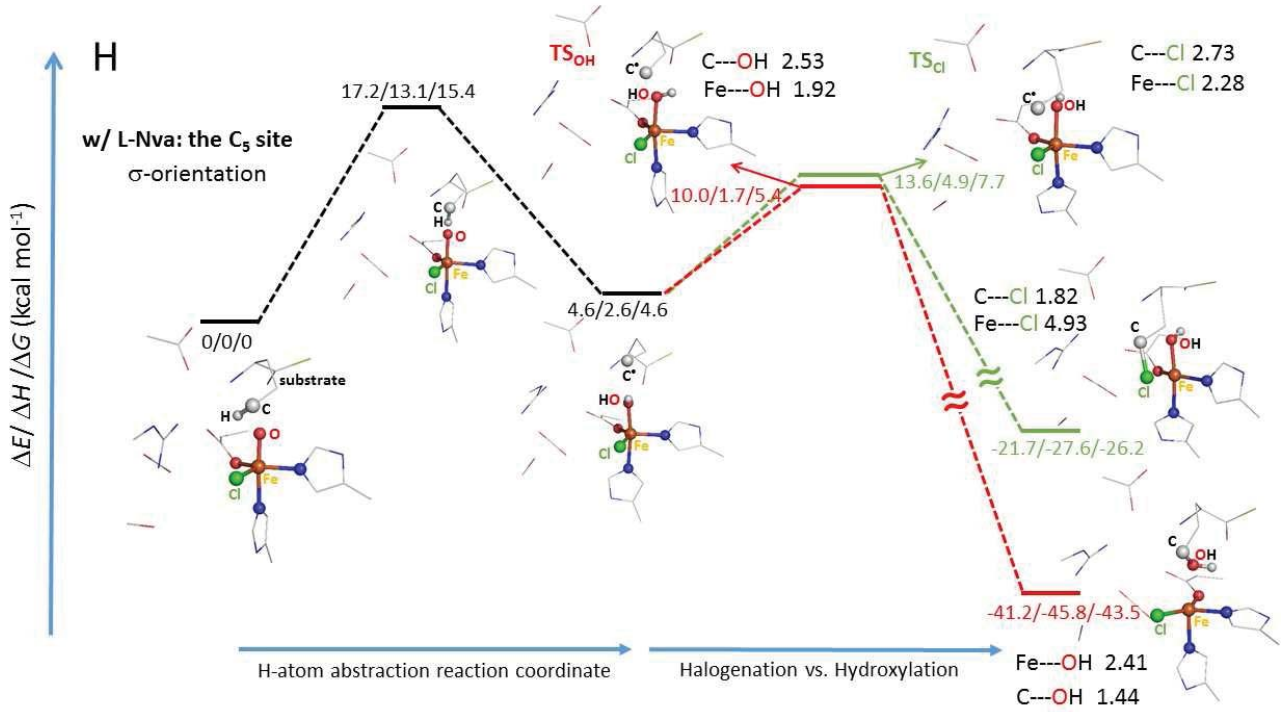
H
w/ L-Nva: the C5 site
σ-orientation
ΔE/ ΔH /ΔG (kcal mol-1)
17.2/13.1/15.4
0/0/0
substrate
TSOH
C---OH 2.53
Fe---OH 1.92
10.0/1.7/5.4
4.6/2.6/4.6
13.6/4.9/7.7
TSCl
C---Cl 2.73
Fe---Cl 2.28
C---Cl 1.82
Fe---Cl 4.93
-21.7/-27.6/-26.2
-41.2/-45.8/-43.5
Fe---OH 2.41
C---OH 1.44
H-atom abstraction reaction coordinate
Halogenation vs. Hydroxylation

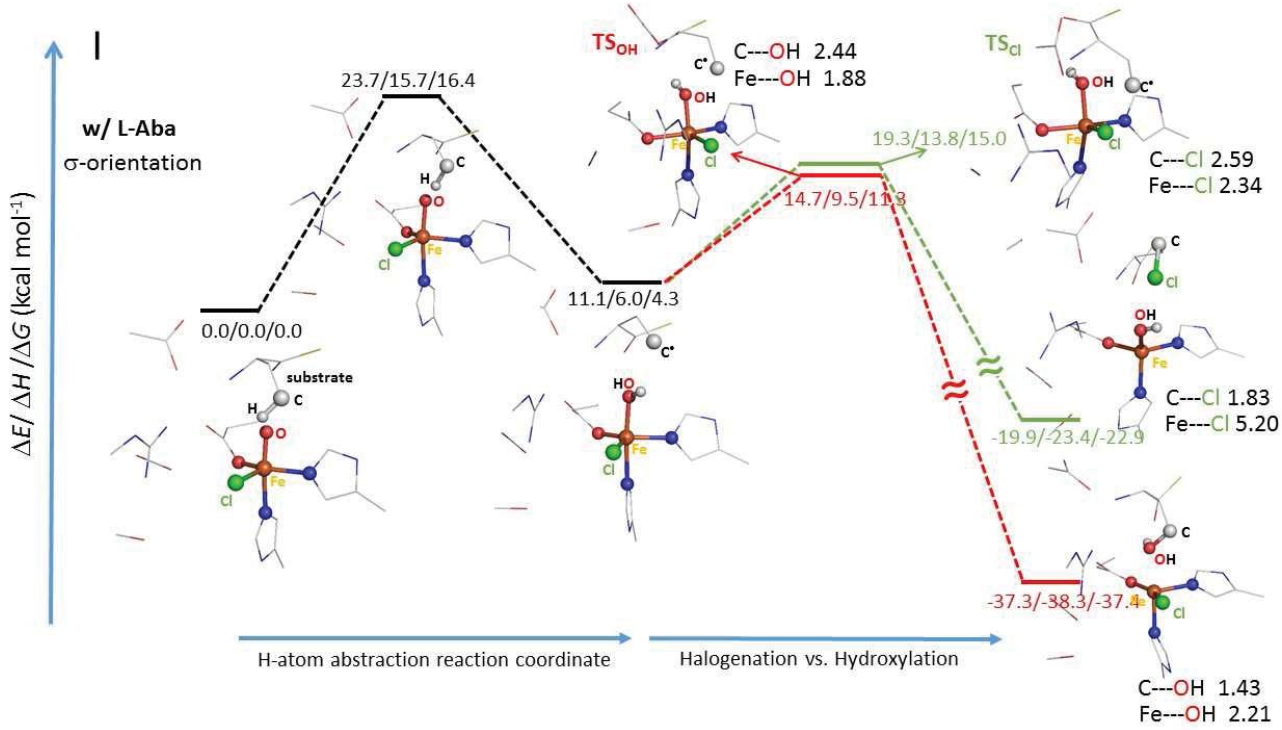

Figure S2: Reaction pathways of chlorination/hydroxylation that follow C—H bond activation (H-atom abstraction) are shown for different substrates (L-Thr, L-Nva and L-Aba) and their different orientations with respect to the initial Fe—oxo bond axis (with the oxo oriented away from the substrate (π-orientation) or toward the substrate (σ-orientation)). Energetics as well as some key geometric parameters are included. The crystallographic water molecule, present in all the structural models, is not displayed.

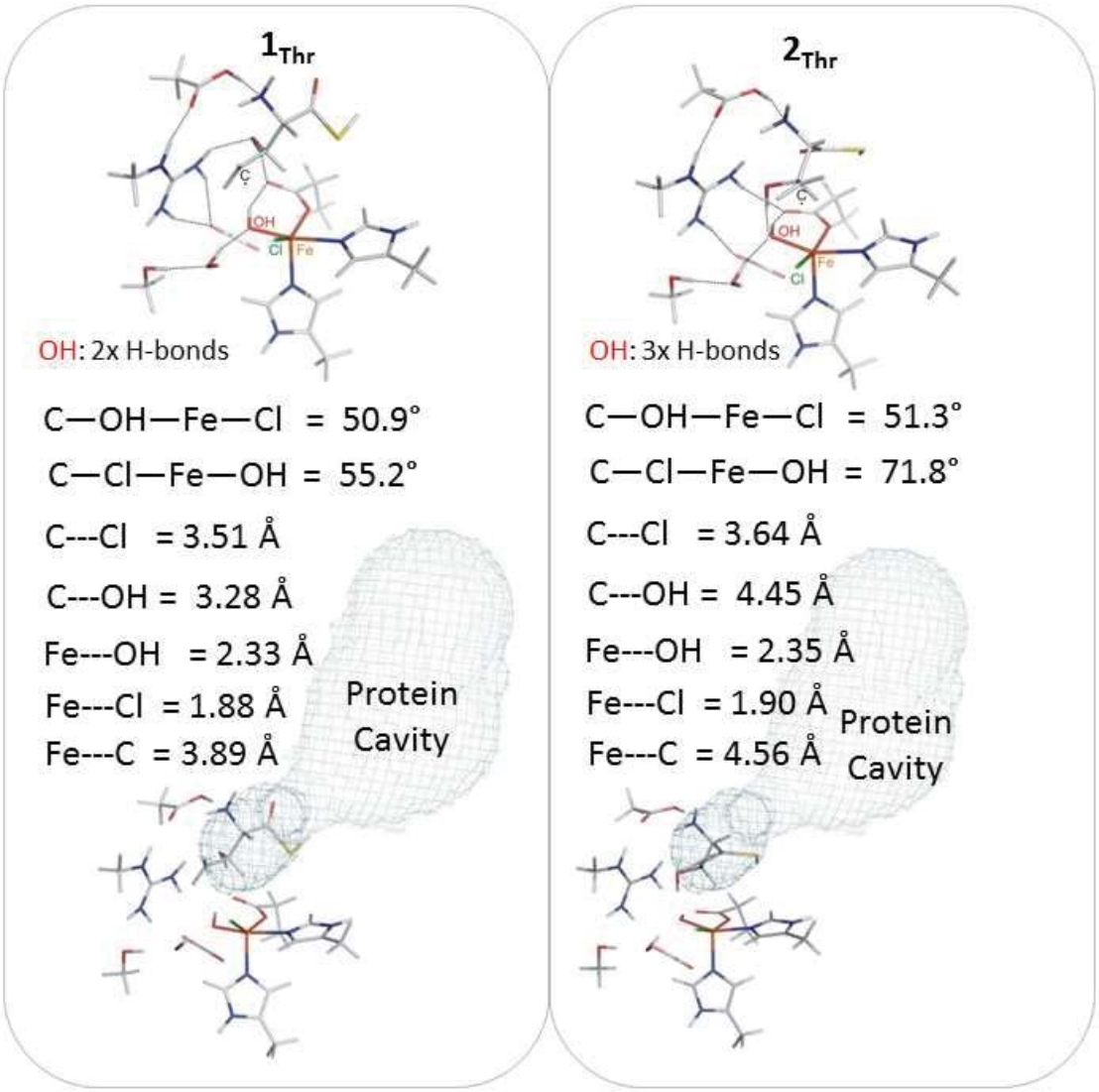

Figure S3A: Geometric comparison of two HO—Fe^{III}—Cl structures $\mathbf{1}_{\mathbf{Thr}}$ and $\mathbf{2}_{\mathbf{Thr}}$. The protein cavity is also depicted (mesh) in order to show that both substrate conformations fit this cavity. Note that the hydroxyl group of the substrate in $\mathbf{1}_{\mathbf{Thr}}$ vs. $\mathbf{2}_{\mathbf{Thr}}$ forms an H-bond with the carboxylate vs. the OH^- ligand, respectively.

For all the substrates used in this study the S atom was kept fixed at the position, which was determined for the native substrate L-threonine according to a molecular docking procedure of Borowski et al (ref 15 in the main text). We note that the S atom can be dislocated from that position along the protein cavity axis depending on the substrate (i.e., closer/further to/from the Cl ligand). However, we anticipate that we would still observe the trends in distortion energy for hydroxylation in **Figure 2** since the hydroxylation trajectory requires a distortion of the system in the direction that is perpendicular to the axis of the cavity. This distortion energy is the key factor contributing to selectivity in SyrB2 (see section 3.2 and discussion in the main text).

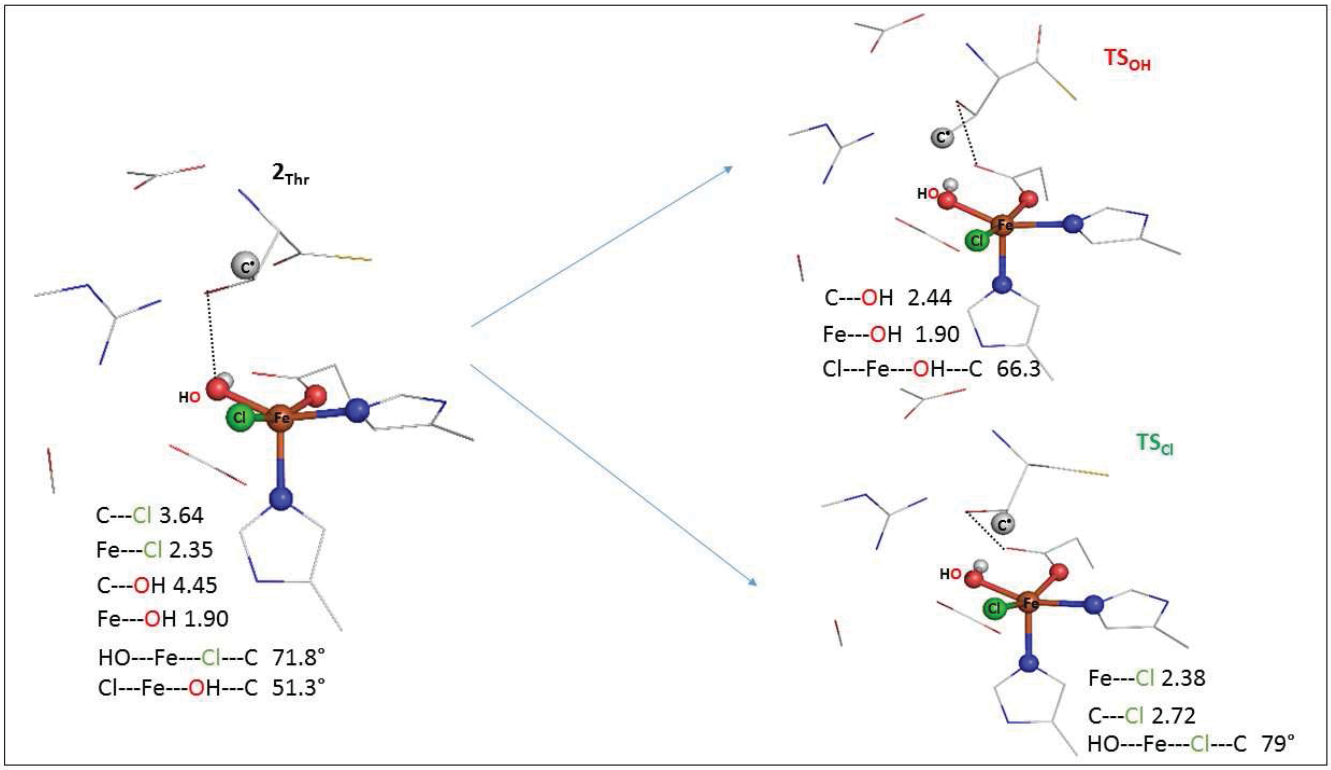

Figure S3B: Expanded $\mathbf{TS_{Cl}}$, $\mathbf{TS_{OH}}$ and $\mathbf{2_{Thr}}$ structures and the key geometric parameters. The crystallographic water molecule, present in all structural models, is not displayed.

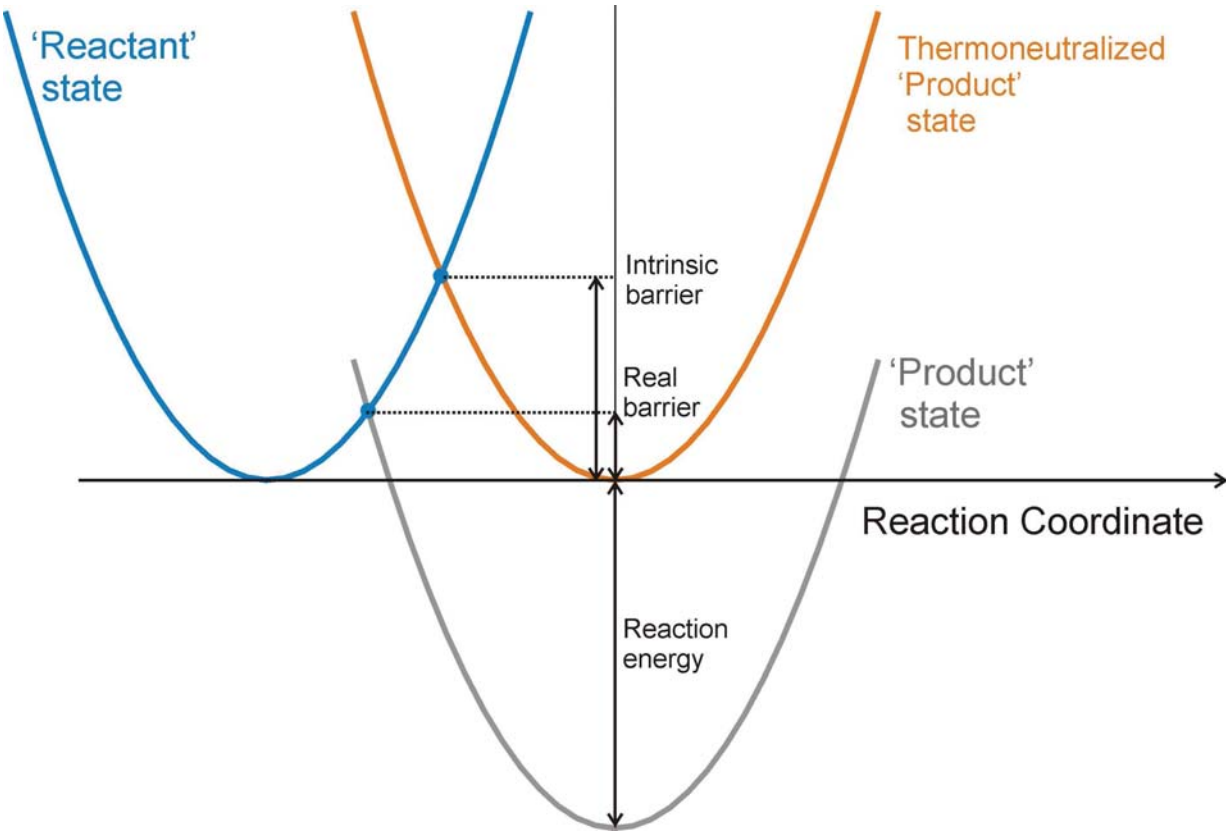

Figure S4A: Marcus theory, originally developed to describe rates of electron transfer reactions and later also applied to atom transfer reactions (see references in the main text), is based on the following assumptions (approximations):

- The potential-energy (or free-energy) surfaces of the 'reactant' and 'product' states have the same parabolic shape.
- The interaction between the electronic 'reactant' and 'product' states along a reaction coordinate is negligible.

Taking into account these approximations, Marcus theory allows for a quantification of the effect of the thermodynamic driving force on the reaction barrier by shifting one parabola (associated with the 'product' state) to energy neutrality (as documented in this figure).

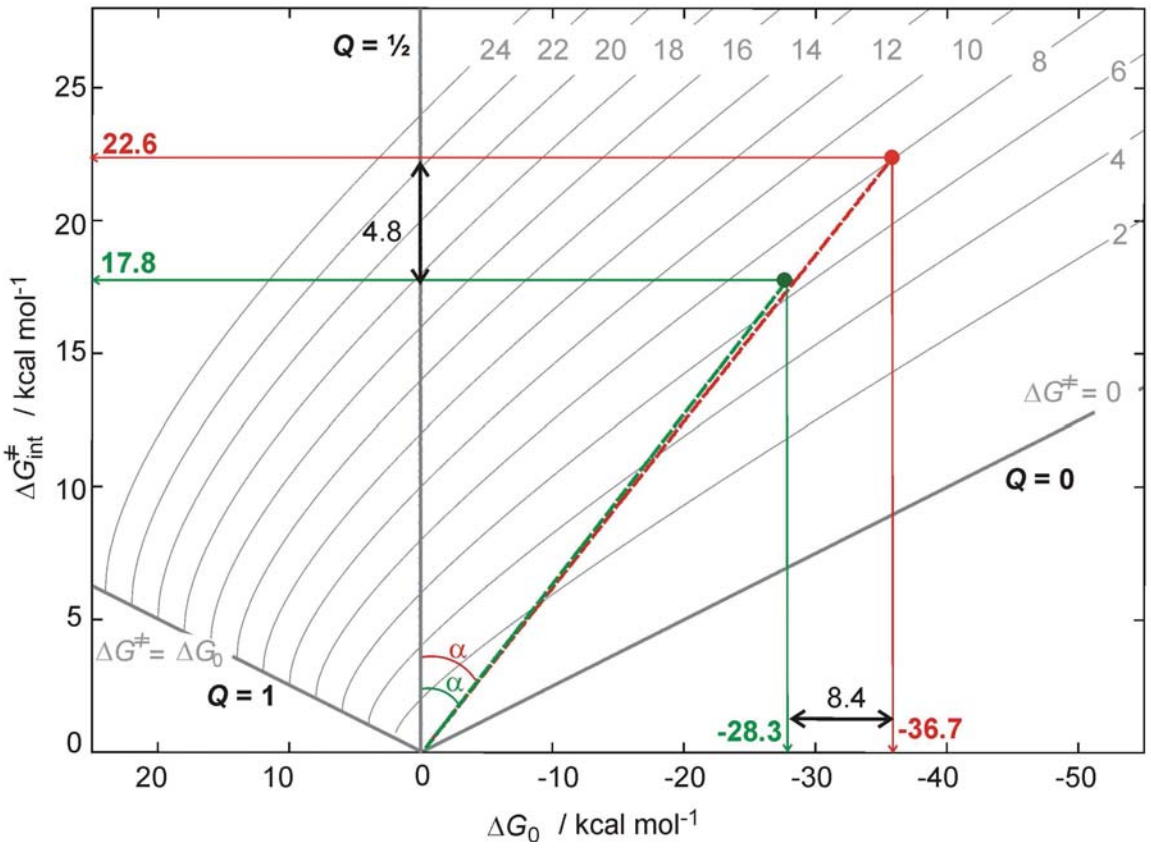

Figure S4B: The isocontour plots of the activation free energy ($\Delta G^{\neq}$), which is, according to Marcus theory, dependent on two variables: the reaction free energy (ΔG_0 along the horizontal axis) and the intrinsic activation free energy ($\Delta G^{\neq}_{int}$ along the vertical axis) [$\Delta G^{\neq} = \Delta G^{\neq}_{int} + \Delta G_0/2 + \Delta G_0^2/(16\times\Delta G^{\neq}_{int})$]. From the computational results for the native substrate L-Thr, from **Figure S2**, the green and red circles positioned at (ΔE_0, $\Delta E^{\neq}$) = (-23.3, 6.5) and (-36.7, 8) in the plot define the intrinsic activation free energies of chlorination and hydroxylation of 17.8 and 22.6 kcal mol^{-1}, respectively. Note that the position of $\mathbf{TS_{Cl}}$ vs. $\mathbf{TS_{OH}}$ along the unitless Marcus reaction coordinate $Q \equiv 0.5 + 1/8\times\mathrm{tg}\alpha \in$ [reactant = 0, product = 1], where $\mathrm{tg}\alpha = \Delta E_0/\Delta E^{\neq}_{int}$, can be also obtained from these plots.

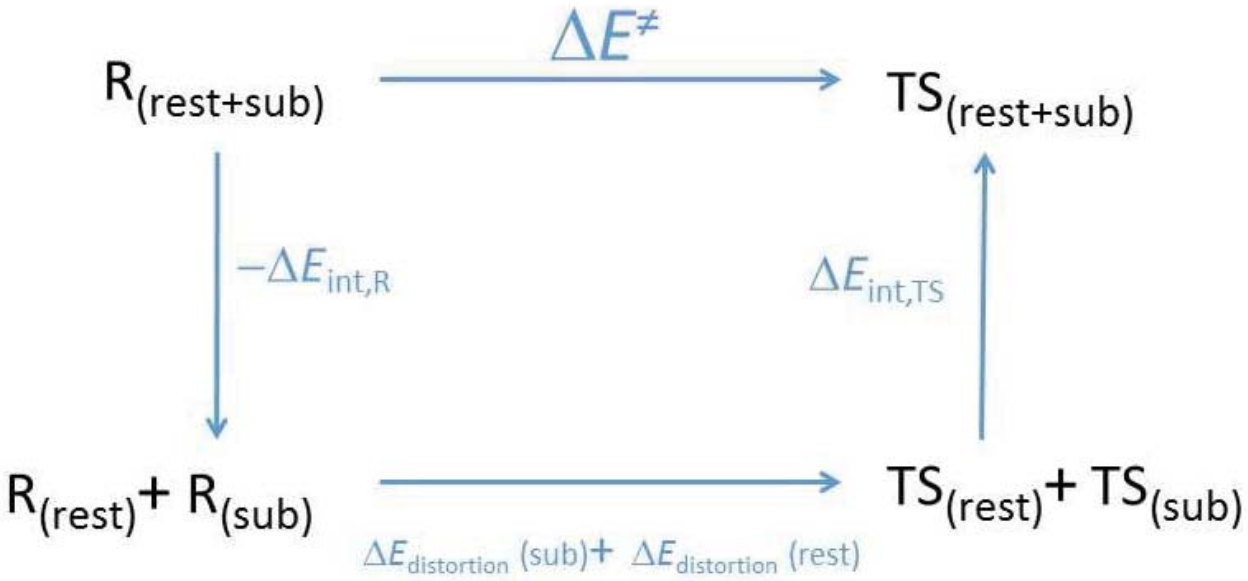

Figure S5. The energy cycle for the transformation of the reactant ($R_{(rest+sub)}$; upper left) to the transition state ($R_{(rest+sub)}$; upper right) comprises the following steps: (*i*) the dissociation energy of the substrate and the active site of SyrB2 (the latter denoted as the "rest"), both kept at their reactant geometries (the left vertical arrow); (*ii*) the distortion energy of the unbound substrate and the rest to reach the transition state geometry (the lower horizontal arrow); and (*iii*) the binding energy of the substrate and the rest, both kept at their transition geometries (the right vertical arrow).

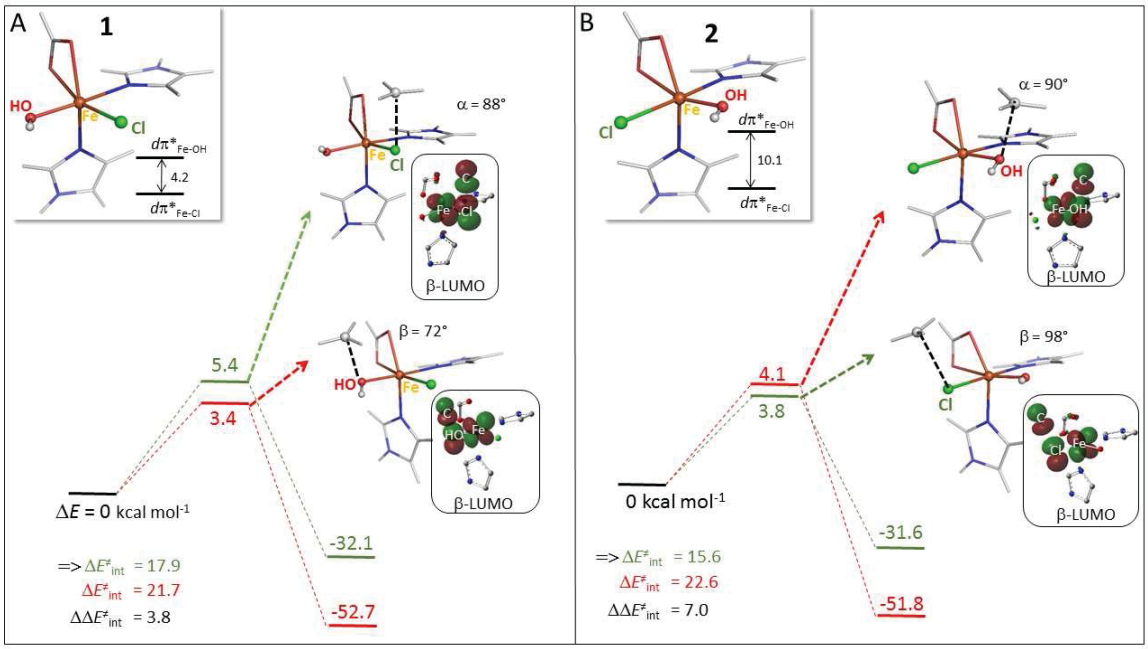

Figure S6. **A.** Chlorination (green) and hydroxylation (red) of the $CH_3^{\bullet}$ substrate by the HO—Fe^{III}—Cl species with Cl^- *trans* to the equatorial carboxylate group and OH^- *trans* to the axial imidazole (model **1**) with its two selectivity-contributing FMOs included in the inset at top. **B.** Chlorination and hydroxylation of the $CH_3^{\bullet}$ substrate by the HO—Fe^{III}—Cl species with OH^- *trans* to the equatorial carboxylate group and Cl^- *trans* to the axial imidazole (model **2**) with FMOs in the inset. Energies are in kcal mol^{-1}. The key TS_{Cl} and TS_{OH} structures starting from **1** and **2**, including the respective β-LUMOs and the intrinsic activation energies ($\Delta E^{\neq}_{int}$) are also shown. For clarity, H atoms in all of structures are not visualized.

Figure S6 has two six-coordinate structures: **1** with its Cl^- ligand *trans* to the coordinated COO^- group (as in SyrB2) and its OH^- *trans* to an imidazole (**Figure S6A**), and **2**, where the Cl^- and OH^- ligands are interchanged (**Figure S6B**). These structures and their corresponding $d\pi^*_{Fe–OH}$ and $d\pi^*_{Fe–Cl}$ FMOs are given in the boxes at the top left of each panel. Upon reaction with the methyl radical, each of these structures orients such that the radical is above the Fe—Cl bond for chlorination (α ~ 90°) or above the Fe—OH bond for hydroxylation (defined by the dihedral angle β [C$^{\bullet}$—OH—Fe—Cl] ~ 90°). The reaction barriers for chlorination (green) vs. hydroxylation (red) are given in the center in both panels of **Figure S6**. Note that the thermodynamics of **1** and **2** are the same (bottom right in both of the panels) with hydroxylation favored by ~20 kcal mol^{-1}. The intrinsic barriers for each reaction are given at the bottom left, where the positive $\Delta\Delta E^{\neq}_{int}$ indicates that chlorination is favored over hydroxylation. Note that chlorination is even more favored than hydroxylation by 3.2 kcal mol^{-1} in **2** relative to **1**. This parallels the FMO energy differences in the boxes at the top where the $d\pi^*_{Fe–Cl}$ orbital is lower in energy for both structures with **2** having a greater energy splitting of the $d\pi^*_{Fe–Cl}$ / $d\pi^*_{Fe–OH}$ FMOs (with the $d\pi^*_{Fe–OH}$ being 5.9 kcal mol^{-1} less stable).

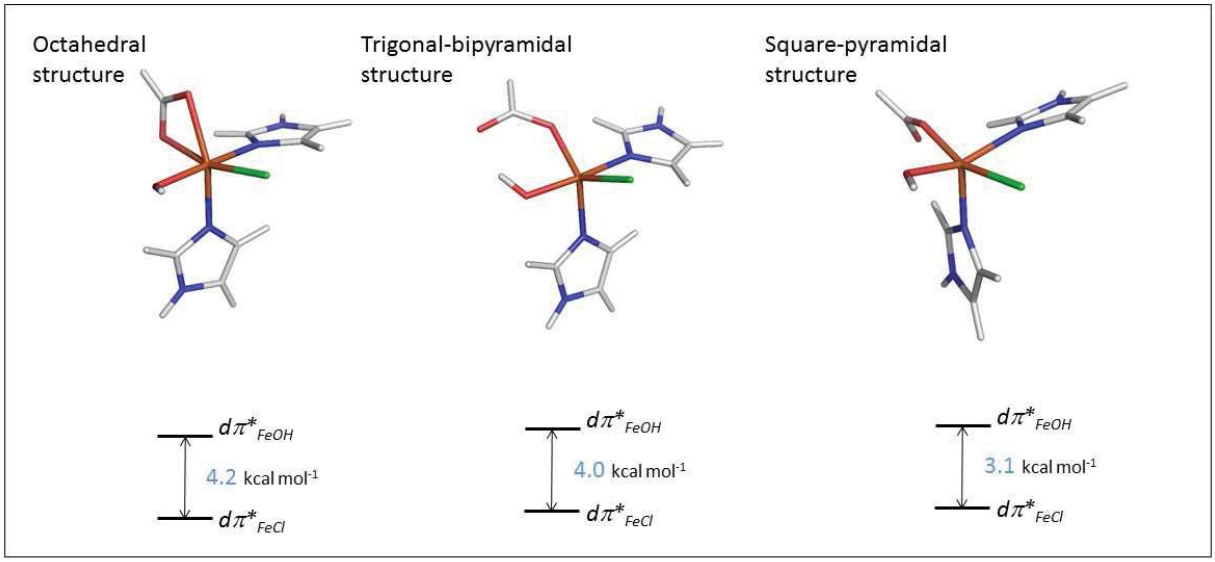

Figure S7: Ligand-field geometries and the associated FMO energy splittings. The dihedral angle O–O–Cl–N, defining the equatorial plane in the square-pyramidal geometry, was kept fixed at 0° during the geometry optimization. The angle HO–Fe–N, defining the z axis in the trigonal-bipyramidal geometry, was kept fixed at 180° during the geometry optimization.

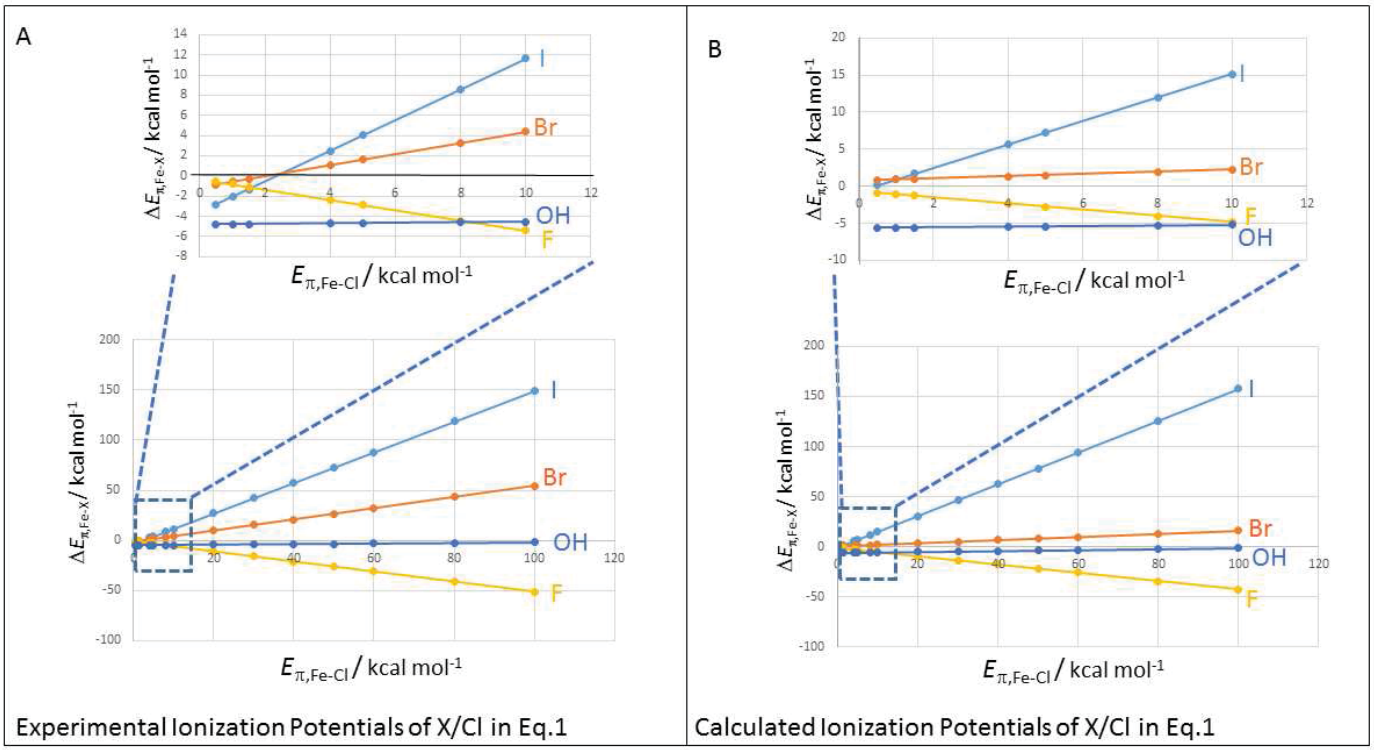

Figure S8: Estimation of the π-donation contribution to the destabilization energy of the $d\pi^*_{Fe–X}$ relative to the contribution of Cl π-donation to the $d\pi^*_{Fe–Cl}$ energy calculated according to eq. 1 (from the main text). From this equation, the relative π-donation contribution $E_{\pi,Fe\text{-}X}$ is the function of $E_{\pi,Fe\text{-}Cl}$. All parameters entering eq. 1 are taken from **Figure 7** (here: for panel **A** and **B**, the experimental and calculated ionization potentials of X/Cl were used, respectively)

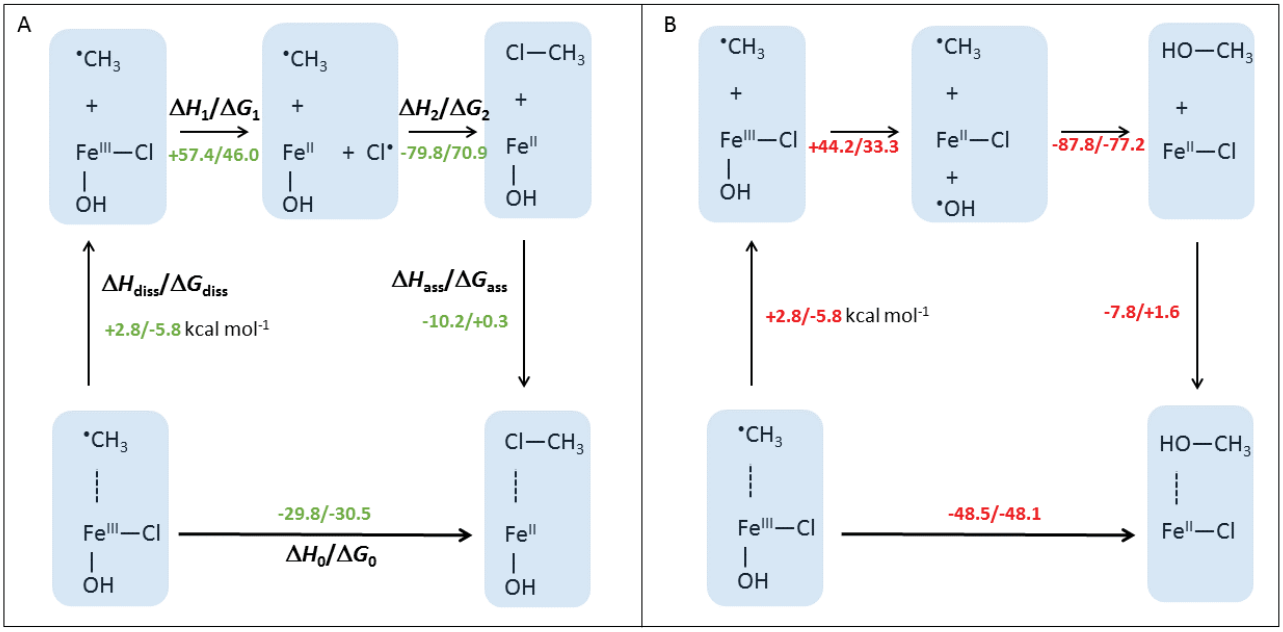

Figure S9. A. The gas-phase thermodynamic cycle for chlorination of the $CH_3^{\bullet}$ substrate by complex **1** (depicted in **Figure S6** in the main text), where the reaction enthalpy/free energy $\Delta H_0/\Delta G_0$ is divided into the enthalpy/free energy of dissociation of $CH_3^{\bullet}$ from **1** ($\Delta H_{diss}/\Delta G_{diss}$), homolytic cleavage of the Fe^{III}—Cl bond in **1** ($\Delta H_1/\Delta G_1$), the formation of the H_3C—Cl bond ($\Delta H_2/\Delta G_2$) and the enthalpy/free energy of the association of H_3C—Cl with the Fe^{II} complex ($\Delta H_{ass}/\Delta G_{ass}$). **B**. The gas-phase thermodynamic cycle for hydroxylation of the $CH_3^{\bullet}$ substrate by complex **1**, analogous to the cycle from panel **A**.

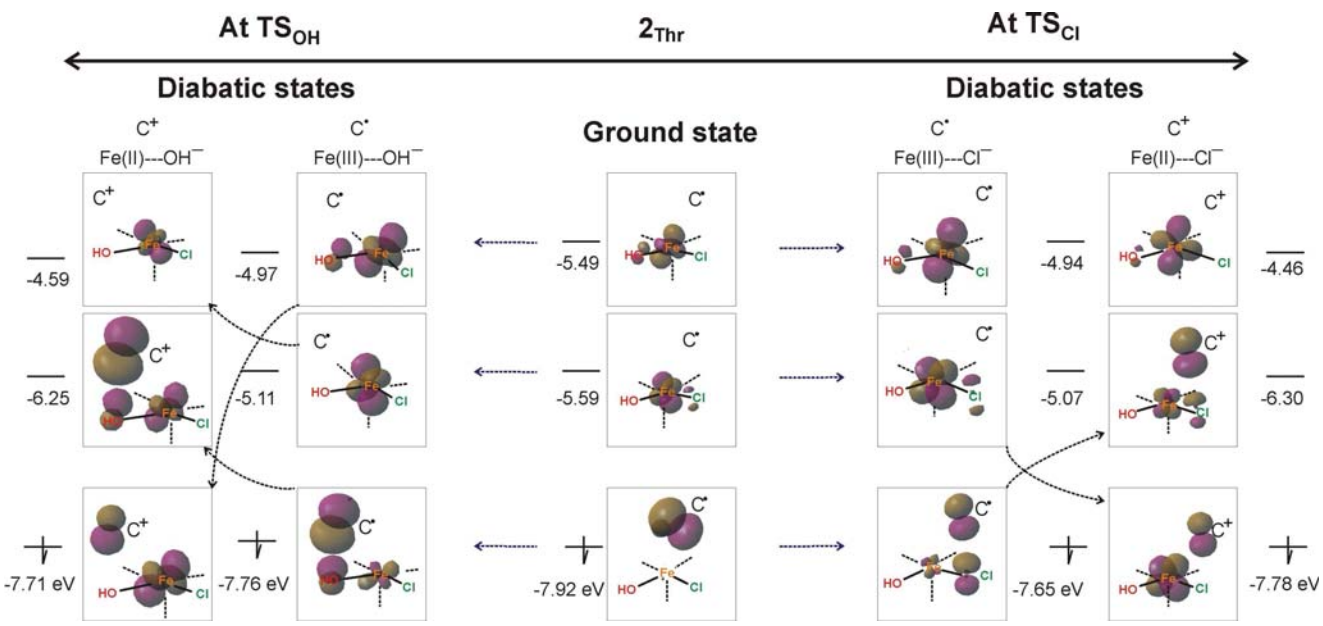

Figure S10. The DFT FMOs (β-HOMO, β-LUMO and β-LUMO+1) associated with the ground-state electronic structure at **2$_{Thr}$** (*middle*). For hydroxylation, the corresponding FMOs that are associated with the cDFT-calculated 'reactant' C$^•$/Fe^{III}—OH$^-$ and 'product' C$^+$/Fe^{III}—OH$^-$ diabatic states at TS$_{OH}$ are shown on the left. For chlorination, the FMOs associated with the cDFT-calculated 'reactant' C$^•$/Fe^{III}—Cl$^-$ and 'product' C$^+$/Fe^{III}—Cl$^-$ diabatic states at TS$_{Cl}$ are on the right of the Figure. For diabatic PESs, see **Figure 9** from the main text.

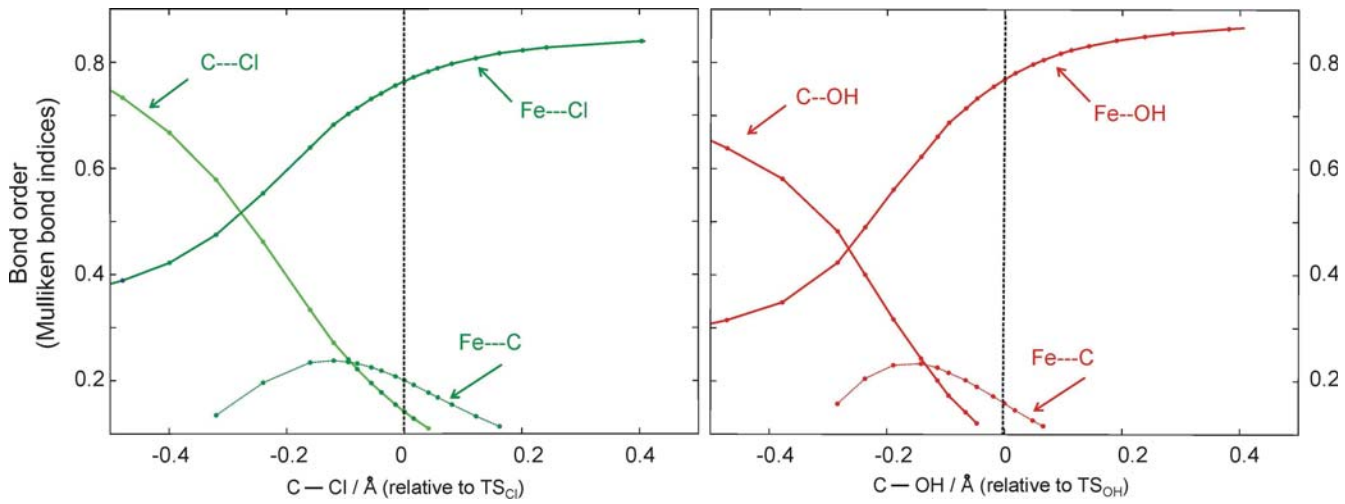

Figure S11. Evolution of three selected Mulliken bond indices that significantly vary along the TS_{Cl} reactive mode (represented by the change in the C—Cl bond length relative to TS_{Cl} in going from right to left (*left panel*)) or along the TS_{OH} reactive mode (represented by the change in the C—OH bond length relative to TS_{OH} in going from right to left (*right panel*)). This Figure is associated with **Figure 9** from the main text.

Table S1. The ability of the ligand X^- to impact the energy of the FMO by π-donation in the $(NH_3)_3(X)Fe^{III}Cl$ complex (structure from **Figure 7** (the main text)) is quantified by the 'destabilization energy' ($E_{\pi,FeX}$) that is estimated as the product of c_x^2 (the weighted admixture of the ligand p_X character in the $d\pi^*_{Fe-X}$ orbital) and Δ (the energy gap between the 'non-interacting' ligand p_X and d_{Fe} orbitals). The Δ splitting was calculated at the cDFT level of theory.

X	Δ^a / eV	c^2	$E_{\pi,FeX}=\Delta\bullet c^2$ / eV	$E_{\pi,FeX}$ / $E_{\pi,FeCl}$
I^-	11.2	0.284	3.17	2.5
Br^-	14.3	0.191	2.73	2.1
Cl^-	15.9	0.081	1.28	1
F^-	22.5	0.064	1.44	1.1
OH^-	8.8	0.115	1.01	0.8

[a]cDFT energies of the 'non-interacting' ligand p_X and metal d orbitals were estimated for $(NH_3)_3(X)Fe^{III}Cl$, where Fe—X was elongated to 6.0 Å. cDFT calculations were constrained to five unpaired electrons on $(NH_3)_3Fe^{III}Cl$ and no spin density at X^-.

Approach presented in section 3.3

From MO theory, the destabilization energy of a metal *d*-orbital due to the (π-)donation from a ligand X is given by:

$$E_{destab,Fe-X} = -c_X^2 \left(E_X - E_{Fe}\right) \quad \textbf{eq. 1}$$

where E_X is the energy of the *p* orbital of halide X (non-interacting with the iron)
and E_{Fe} is the energy of the *d* orbital of the Fe complex (without X).

E_X equals approximately to the negative value of the ionization potential of X (Koopmans' theorem):

$$E_X \equiv E\left(p_X\right) \approx -I_X \quad \textbf{eq. 2}$$

and E_{Fe} equals approximately to the negative value of the ionization potential of this complex:

$$E_{Fe} \equiv E\left(d_{Fe}\right) \approx -I_{Fe} \quad \textbf{eq. 3}$$

Then,

$$E_{destab,Fe-X} \cong c_X^2 \left(I_X - I_{Fe}\right) \quad \textbf{eq. 4}$$

Now, the idea is to calculate the ionization potential of X^- (and avoid of the explicit calculation of the ionization potential of the Fe complex in the absence of X). For this purpose, the ionization potential I_{Fe} is taken as a function of $E_{destab,Fe-X}$ using the following equation (analogous to **eq. 4**).

$$E_{destab,Fe-Cl} \cong c_{Cl}^2 \left(I_{Cl} - I_{Fe}\right) \quad \textbf{eq. 5}$$

$$\Rightarrow \quad I_{Fe} \cong \frac{c_{Cl}^2 I_{Cl} - E_{destab,Fe-Cl}}{c_{Cl}^2} \quad \textbf{eq.6}$$

Then, inserting **eq. 6** into **eq. 4** gives:

$$\Delta E_{destab,FeX-FeCl} \cong c_X^2 \left(I_X - \frac{c_{Cl}^2 I_{Cl} - E_{destab,Fe-Cl}}{c_{Cl}^2} \right) - E_{destab,FeCl}$$

that is finally modified to:

$$E_{\pi,Fe-X} - E_{\pi,Fe-Cl} = \Delta E_{\pi,Fe-X} \cong c_X^2 \left(I_X - I_{Cl}\right) + E_{\pi,Fe-Cl} \left(\frac{c_X^2}{c_{Cl}^2} - 1 \right)$$

Table S2. The selected AO contributions to the β-HOMO as calculated at the TS_{Cl} with different substrates (the y axis is along the Fe—Cl bond; the x axis is along the Fe—OH bond as defined in **Figure 3A** in the main text). The weight of the d_{xy} in the β-HOMO increases with the decrease in the angle α (defined in **Figure 4A** in the main text).

System	The angle α	%C(*p*)	**%d_{yz}**	%d_{xz}	**%d_{xy}**
NvaC5	44	58.6	**12.5**	0.7	**7.4**
1_{Thr}	49.6	39.4	**25.3**	0.6	**6.8**
Aba	51	43	**22.3**	0.7	**6.2**
NvaC4	62	41.3	**25.6**	0.1	**1.2**
2_{Thr}	78.6	47.1	**23.7**	0	**0.2**

Table S3. The dihedral angles β[= H_{OH}—O_{OH}—Fe—Cl] and γ [= H_{H2O}—O_{OH}—Fe—Cl] at the reactant and TS_{OH} geometries.

System	The angle β[R]	The angle β[TS_{OH}]	The angle γ[R]	The angle γ[TS_{OH}]
NvaC5	152.9°	166.3°	38.7°	39.3°
1_{Thr}	137.5°	164.1°	41.8°	48°
Aba	140.8°	166.8°	40.5°	47.7°
NvaC4	166°	176.4°	28.3°	51.3°
2_{Thr}	173.2°	164.1°	52.8°	48°